ACS Catalysis

Research Article

pubs.acs.org/acscatalysis

In Situ Spectroscopic Characterization of $Ni_{1-x}Zn_x/ZnO$ Catalysts and Their Selectivity for Acetylene Semihydrogenation in Excess Ethylene

Charles S. Spanjers,[†] Richard S. Sim,[†] Nicholas P. Sturgis,[†] Bernd Kabius,[‡] and Robert M. Rioux*[,†,§]

[†]Department of Chemical Engineering, [‡]Materials Research Institute, and [§]Department of Chemistry, The Pennsylvania State University, University Park, Pennsylvania 16802, United States

Supporting Information

ABSTRACT: The structures of ZnO-supported Ni catalysts were explored with in situ X-ray absorption spectroscopy, temperature-programmed reduction, X-ray diffraction, high-resolution transmission electron microscopy (HRTEM), scanning transmission electron microscopy, and electron energy loss spectroscopy. Calcination of nickel nitrate on a nanoparticulate ZnO support at 450 °C results in the formation of Zn-doped NiO (ca. $Ni_{0.85}Zn_{0.15}O$) nanoparticles with the rock salt crystal structure. Subsequent in situ reduction monitored by X-ray absorption near-edge structure (XANES) at the Ni K edge reveals a direct transformation of the Zn-doped NiO nanoparticles to a face-centered cubic alloy, $Ni_{1-x}Zn_x$, at ~400 °C with x increasing with increasing temperature. Both in situ XANES and ex situ HRTEM provide evidence for intermetallic β_1-NiZn formation at ~550 °C. In comparison to a Ni/SiO_2 catalyst, Ni/ZnO necessitates a higher temperature for the reduction of Ni^{II} to Ni^0, which highlights the strong interaction between Ni and the ZnO support. The catalytic activity for acetylene removal from an ethylene feed stream is decreased by a factor of 20 on Ni/ZnO in comparison to Ni/SiO_2. The decrease in catalytic activity of Ni/ZnO is accompanied by a reduced absolute selectivity to ethylene. H−D exchange measurements demonstrate a reduced ability of Ni/ZnO to dissociate hydrogen in comparison to Ni/SiO_2. These results of the catalytic experiments suggest that the catalytic properties are controlled, in part, by the zinc oxide support and stress the importance of reporting absolute ethylene selectivity for the catalytic semihydrogenation of acetylene in excess ethylene.

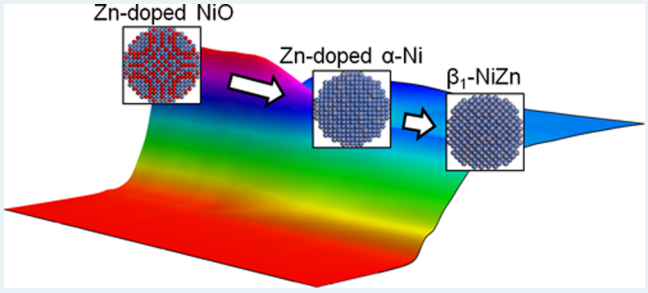

KEYWORDS: *nickel, zinc oxide, X-ray absorption spectroscopy, reduction, acetylene, semihydrogenation*

1. INTRODUCTION

The production of ethylene from steam cracking of naphtha generates acetylene impurities as a byproduct typically at a level of 0.5−2%. Acetylene must be reduced to less than 5 ppm to prevent deactivation of the ethylene polymerization catalyst.[1,2] Pd/Al_2O_3 or Pd/SiO_2 with low metal loadings (ca. 0.5%) is widely used for the upgrading of olefins but does not provide sufficient selectivity to warrant use in acetylene hydrogenation, as a result of overhydrogenation to ethane and oligomer ("green oil") formation.[3,4] To achieve high ethylene selectivity, cofeeding of CO or modification of the catalyst with Ag is required. The addition of Ag to Pd decreases hydrogen coverage, resulting in a lower propensity for overhydrogenation and ultimately higher ethylene selectivity.[4−12] Since the first patent on Pd−Ag catalysts in 1957,[13] Pd−Ag remains the optimal catalyst for this process. However, there has been recent interest to improve on the current technology in terms of both catalyst selectivity and cost. Intermetallic Pd−Ga compounds demonstrate an increased ethylene selectivity in comparison to Pd−Ag as a result of electronic modification and isolation of the active sites of Pd.[14−18] However, since catalyst cost is still a concern, there is interest in replacing Pd-based catalysts with low-cost, earth-abundant elements.

Replacement of Pd with an active component from the late 3d transition metals such as Fe, Cu, and Ni poses unique challenges that can be overcome through the addition of a second metal. For example, Fe catalysts require a pressure of at least 50 bar and a temperature of 100 °C for the hydrogenation of unsaturated C−C bonds.[19] Modification of Fe with Al to form intermetallic $Al_{13}Fe_4$ was recently shown to exhibit high selectivity for acetylene hydrogenation as a result of site isolation and alteration of the electronic structure of Fe due to chemical bonding.[19] Cu-based hydrogenation catalysts tend to form oligomerization products but have been made more selective through the addition of Ni, which increases the catalyst's ability to dissociate hydrogen.[20−22] Ni-based catalysts suffer from both their ability to overhydrogenate and their tendency to oligomerize alkynes.[23−27] Studt et al. identified Ni−Zn using density functional theory (DFT) as a good alkyne semihydrogenation catalyst and provided experimental evidence that the addition of Zn to a supported $Ni/MgAl_2O_4$ catalyst reduces the formation of ethane during acetylene

Received: August 29, 2014
Revised: April 11, 2015
Published: April 14, 2015

DOI: 10.1021/acscatal.5b00627
ACS Catal. 2015, 5, 3304−3315

hydrogenation in the presence of excess ethylene; however, no measure of oligomerization or ethylene selectivity was presented in this study.[28] Recent work from our group has shown that bulk intermetallic Ni−Zn compounds reduce the formation of oligomeric compounds as a result of a decreased binding energy of acetylene, thereby boosting the selectivity to ethylene.[29] As a result of the low surface areas and correspondingly low acetylene-removal rates of the most selective bulk intermetallic Ni−Zn catalysts, there exists a need to create highly dispersed Ni−Zn catalysts.

Synthesis of supported intermetallic Ni−Zn catalysts is difficult, due to the oxophilic nature and volatility of Zn. ZnO does not reduce under the presence of hydrogen, and instead ZnO sublimes at temperatures of approximately 600 °C.[30] Evidence for the formation of an intermetallic Ni−Zn compound was not reported in either of the previous studies using coimpregnation of Ni and Zn on a $MgAl_2O_4$ support.[28,31] Similarly, Ni−Zn catalysts derived from hydrotalcite-like precursors show no evidence for the formation of intermetallic Ni−Zn compounds.[32−34] Furthermore, the amount of reduced Ni is lower in Zn-containing catalysts in comparison to catalysts without Zn, which stresses the difficulty in creating intermetallic Ni−Zn from divalent precursors.[33] However, using ZnO as a support for Cu results in the reduction of ZnO and formation of a Cu−Zn alloy with the face-centered cubic structure.[35] Pd/ZnO and Pt/ZnO catalysts promote the facile reduction of the ZnO support under hydrogen, forming intermetallic PdZn and PtZn, respectively.[36−42] Applications for Ni/ZnO catalysts beyond selective hydrogenation include hydrodeoxygenation and hydrodearomatization,[43] methanol[44] and ethanol steam re-forming,[45] and hydrodesulfurization.[46−49] Of these Ni/ZnO catalysts, neither alloy nor intermetallic formation was observed in two cases,[43,47] while Ni−Zn alloy formation was observed in two cases,[46,49] and intermetallic β_1-NiZn was clearly identified by Petzold et al.[48] However, in the study by Petzold and co-workers it is unclear whether the intermetallic NiZn phase formed during the reduction or reaction step.

Herein, we report X-ray absorption near-edge structure (XANES) characterization during the in situ reduction of Ni/ZnO catalysts prepared from wet impregnation of nickel nitrate on a moderate surface area (41 m^2/g) ZnO support. The in situ characterization is combined with ex situ characterization to obtain a complete picture of the structure of the Ni/ZnO catalysts after the calcination and reduction steps. We measured the catalytic selectivity for acetylene semihydrogenation in excess ethylene and the activity for H−D exchange to understand the effect of alloy formation and the ZnO support on the catalytic properties of Ni/ZnO catalysts. The beneficial catalytic properties derived from the formation of intermetallic NiZn are offset by acetylene oligomerization on ZnO, leading to a poor catalyst for acetylene semihydrogenation.

2. EXPERIMENTAL SECTION

2.1. Synthesis of Supported Catalysts. Ni/ZnO catalysts were synthesized by dissolving $Ni(NO_3)_2{\cdot}6H_2O$ (Sigma-Aldrich) in Milli-Q water and adding to nanoscale ZnO powder (NanoActive ZnO, NanoScale Corp, Manhattan, KS) using the wet impregnation technique. In a representative synthesis of 2 wt % Ni/ZnO, 0.5 g of $Ni(NO_3)_2{\cdot}6H_2O$ was dissolved in 7 mL of Milli-Q water and added to 4.9 g of ZnO powder. Weight loadings are defined as the mass of Ni divided by the total mass of Ni and ZnO in the catalyst sample. Samples were dried for 12 h at 110 °C followed by calcination at 450 °C for 4 h. A 2 wt % Ni/SiO_2 catalyst was prepared by dissolving 0.01 g of $Ni(NO_3)_2{\cdot}6H_2O$ in 10 mL of Milli-Q water and adding the solution to 1 g of Cabot CAB-O-SIL HS-5 silica. The mixture was stirred thoroughly, dried at 110 °C for 12 h, and calcined at 450 °C for 4 h. Actual weight loadings for the Ni/ZnO samples were determined with ICP-OES using an aqua regia digestion (which dissolves both NiO and ZnO) and are 0.50 ± 0.02, 0.99 ± 0.04, 1.97 ± 0.04, 4.8 ± 0.2, and 9.8 ± 0.4 wt % for the nominal 0.5, 1, 2, 5, and 10 wt % catalysts, respectively.

2.2. Synthesis of Bulk Intermetallic Compounds. Bulk intermetallic Ni−Zn compounds were synthesized as reference materials for X-ray absorption spectroscopy, following a previously reported procedure.[29] Ni powder (Sigma-Aldrich, <150 μm, 99.999%) and Zn granules (Sigma-Aldrich, 3 mm diameter, 99.99%) were placed in alumina crucibles (LSP Ceramics, 13 mm i.d.) in the correct stoichiometry and sealed in quartz tubes evacuated to 30 mTorr. Ni_5Zn_{21} and NiZn were heated at a rate of 10 °C/min to 700 °C, held for 24 h, and cooled to room temperature at a rate of 1 °C/min. Ni_4Zn was heated at a ramp rate of 10 °C/min to 900 °C, held for 24 h, and cooled to room temperature at a ramp rate of 3 °C/min. A stainless steel ball mill (SPEX Mixer/Mill, 8001 sample container) was used to mill the samples. Samples were loaded into the ball mill in an argon-filled glovebox, and 1 mL of 1,1,1,2,2,3,4,5,5,5-decafluoropentane (Vertrel XF, Dupont) per gram of sample was placed in the milling container prior to milling for 4 h. After milling, the decafluoropentane was allowed to evaporate at room temperature. NiZn and Ni_5Zn_{21} were resealed in evacuated quartz tubes and annealed at 500 °C for 7 days. X-ray diffraction of these compounds shows that phase-pure intermetallic compounds were synthesized.

2.3. In Situ X-ray Absorption Spectroscopy. X-ray absorption spectroscopy (XAS) measurements were performed at beamline X19A of the National Synchrotron Light Source (NSLS) at Brookhaven National Laboratory (Upton, NY). NiO, ZnO, Ni_4Zn, NiZn, and Ni_5Zn_{21} standards were prepared by spreading powder on adhesive polyimide tape and folding such that the step height at the Ni K edge (8333 eV) was ∼1.0. Ex situ measurements of catalyst samples were performed on samples prepared either by spreading powder on adhesive polyimide tape or by hand pressing a 4 mm o.d. pellet into a stainless steel holder. In situ reduction was performed with a hand-pressed pellet of pure catalyst sample in a 4 mm o.d. stainless steel holder. The edge step for the 2 wt % Ni/ZnO sample was ∼0.4. The calculated total absorption for this sample is ∼3 absorption lengths. A K-type thermocouple was inserted into a small hole in the stainless steel holder ∼5 mm away from the catalyst pellet. The stainless steel holder was placed inside a 2.54 cm o.d. quartz tube sealed with polyimide film and Swagelok Ultra Torr fittings and equipped with an inlet and outlet for the passage of gases. The quartz tube was placed within a tube furnace with a programmable temperature controller. The catalyst pellet was placed at the center of the X-ray beam. Transmission geometry was used for all experiments. The incoming and outgoing X-ray beams were measured with ionization chambers placed before and after the sample. A reference Ni foil was placed between the transmission and reference ionization chambers for measurements at the Ni K edge. Data were acquired from 150 eV before the edge to 980 eV after the edge. The total time for a single scan was ∼15 min. For the in situ reduction, the sample was heated from room

DOI: 10.1021/acscatal.5b00627
ACS Catal. 2015, 5, 3304−3315

temperature to 800 °C at a rate of 1.3 °C/min under a 50 mL/min flow of 5% H_2 balanced with He. Since the temperature was changing over the course of each individual scan, the reported temperatures are the average temperature for each scan.

2.4. Ex Situ Laboratory X-ray Diffraction. Powder X-ray diffraction (XRD) measurements were performed on a PANalytical Empyrean X-ray diffractometer using Cu Kα (λ = 1.5418 Å) radiation. The powder samples were placed in the cavity of a silicon zero-background holder and leveled with a glass slide. The Empyrean is equipped with a PIXcel detector using scanning line mode detection, and the diffractometer radius is 240 mm. Incident beam optics were configured with a 1/2° antiscatter slit, 10 mm beam mask, 1/4° fixed divergence slit, and 0.04 rad soller slits. Diffracted beam optics were configured with 0.04 rad soller slits, a Ni beta filter, and a 1/4° antiscatter slit. Survey diffractograms were acquired with a 2θ step size of 0.025° with a range from 20 to 90° 2θ. High-resolution scans with a longer time step were collected from 39 to 46° 2θ. The diffractometer was checked weekly by measuring the lattice parameter of a NIST 640d Si standard reference material. The deviation from the true lattice parameter of the standard is always less than 0.001 Å, and thus the error on lattice parameters determined from the XRD measurements is assumed to be less than 0.001 Å. The instrumental broadening parameter used in the Scherrer equation for calculation of particle size was determined from the diffraction pattern of the NIST 640d Si standard reference material. For determination of lattice parameters, Rietveld refinement of the XRD data was performed within Jade (Materials Data Incorporated). The error estimate reported for each lattice parameter is either the standard deviation in lattice parameter determined from Rietveld refinement or the instrumental accuracy (0.001 Å), whichever is greater.

2.5. Ex Situ Synchrotron X-ray Diffraction and Pair Distribution Function (PDF) Analysis. Synchrotron X-ray diffraction and pair-distribution function analysis was performed at beamline 11-ID-B at the Advanced Photon Source (APS) at Argonne National Laboratory (Lemont, IL). Measurements were performed at room temperature with an X-ray wavelength of 0.2127 Å, a 0.2 × 0.2 mm X-ray beam size, and a Q_{max} value of 24 Å^{-1}. Two-dimensional (2D) X-ray diffraction patterns were acquired with a General Electric amorphous silicon flat panel detector.[50] Samples were prepared for analysis by filling a polyimide capillary (1 mm i.d.) and sealing with epoxy. The raw 2D X-ray data were integrated radially using FIT2D.[51] The data were subsequently processed using PDFGetX2[52] to remove the background, normalize, and calculate the Fourier transform resulting in the PDF, $G(r)$. The calcined catalyst samples were analyzed by subtracting the empty polyimide capillary PDF. Subsequently, the experimental PDF of pure calcined ZnO was subtracted from the sample PDF. This was done by first adjusting the ZnO PDF with a multiplier and a power expression, aR^b, where a and b are fitted constants. This was done to account for different amounts of ZnO in each sample and particle sizes which differ from the reference spectrum. The grain sizes of the ZnO nanoparticles increased with increasing Ni weight loading, requiring the power expression to subtract the ZnO contribution from each of the PDFs. The PDFs for samples that were calcined and reduced were prepared in a similar manner. After subtraction, $G(r)$ was fitted using PDFGUI[53] with NiO (NaCl structure) and Ni (FCC structure) phases for the calcined and reduced samples, respectively. ZnO was also fitted to each of the samples.

2.6. Temperature-Programmed Reduction. Temperature-programmed reduction (TPR) was performed using a Micromeritics AutoChem 2910 instrument. A 300 mg portion of the sample was added to a U-shaped quartz tube and supported with quartz wool. Samples were heated from room temperature to 600 °C at a rate of 10 °C/min under 3.88% H_2 balanced with Ar at a flow rate of 50 mL/min. Hydrogen uptake was monitored using a thermal conductivity detector (TCD) on the basis of the differences in thermal conductivity of hydrogen and argon. Calibration was performed by measuring the hydrogen uptake of a known amount of copper(II) oxide. The raw signal was converted to the rate of hydrogen consumption using the calibration and hydrogen flow rate.

2.7. Transmission Electron Microscopy. Samples were prepared for transmission electron microscopy (TEM) by sonicating the catalyst powders in ethanol and dropping onto a carbon-coated copper TEM grid. The reduced samples were prepared in a nitrogen-filled glovebox with an oxygen level of less than 1 ppm and transferred to the TEM in a sealed plastic bag. The samples were exposed to atmospheric oxygen for approximately 1 min during sample loading. Diffraction contrast imaging was performed on a JEOL 2010F field emission TEM operated at 200 keV. High-resolution TEM imaging (HRTEM) was performed using a FEI TITAN 3GS instrument operated at 80 and 200 keV. Elemental maps were calculated from spectrum images recorded in scanning TEM (STEM) mode by electron energy loss spectroscopy (EELS). Fourier transforms of high-resolution images were used for phase identification from lattice plane distances.

2.8. Catalysis Measurements. Catalytic selectivity for acetylene semihydrogenation in excess ethylene was determined using a batch reactor. A 2 wt % Ni/ZnO (200 mg) or Ni/SiO_2 (15 mg) sample was loaded into a 1/2 in. o.d. quartz reactor tube, supported by a plug of quartz wool on both sides. Catalysts were reduced in the reactor prior to catalysis under a flow of 50 mL/min 3.88% H_2/Ar by heating at a ramp rate of 10 °C/min to the desired temperature. After the desired temperature was reached, the samples were cooled to room temperature under flowing 3.88% H_2/Ar. Complete details of the experimental protocol for the catalytic measurements may be found in prior work.[29] Briefly, the reactor was evacuated to a pressure of ∼100 mTorr prior to admission of the reactants. $^{13}C_2H_2$ was added to the reactor with a needle valve to a pressure of ∼5 Torr (the starting pressure of acetylene slightly varied, and the actual starting pressure for each experiment may be read from starting acetylene pressure in each plot). Subsequently, 10% H_2/He was added to the reactor to a pressure of 267 Torr, and 10% C_2H_4/He was added to reach a final pressure of 800 Torr. Reactants were circulated at a flow rate of ∼50−100 mL/min using a diaphragm circulation pump. Samples were removed from the reactor with a 50 μL gastight syringe (Hamilton) and analyzed with a Shimadzu GCMS-QP2010 Ultra gas chromatograph (GC) equipped with a mass spectrometer (MS). After two samples were taken at room temperature to establish the initial concentration of acetylene, the reactor was heated to 160 °C over the course of 10 min.

H−D exchange experiments were performed in a 1/2 in o.d. plug flow reactor, using amounts of catalyst identical with those in the acetylene semihydrogenation experiments. The catalysts were reduced under flowing H_2 (10 mL/min) and D_2 (10 mL/

DOI: 10.1021/acscatal.5b00627
ACS Catal. 2015, 5, 3304−3315

min) in the reactor and were cooled to room temperature under an equimolar flow of H_2 and D_2. This procedure ensures equal concentration of H and D on the catalyst surface prior to the H−D exchange measurements. The reactor was subsequently heated at a rate of 3 °C/min to obtain temperature dependence of the H−D exchange. The concentrations of H_2 and HD were measured every 3−4 min by removing 50 μL samples with a syringe from the exit of the reactor and injecting into the mass spectrometer. Because the mass spectrometer uses He as a carrier gas, m/z 4 could not be used to detect D_2 and a mole balance was used to calculate the amount of D_2 from the H_2 and HD concentrations.

3. DATA ANALYSIS

Energy calibration of the XAS data was performed by aligning all scans with the reference foil (8333 eV for Ni K edge) prior to further processing. The IFEFFIT package was used for data normalization and processing.[54,55] Background removal was performed using an Rbkg value of 1.0, a k weight of 2, a pre-edge range of −150 to −30 eV, a normalization range of 150−980 eV, and a spline range of 0−16 k for all samples. The X-ray absorption near-edge structure (XANES) region was selected for factor analysis, since it is relatively insensitive to the temperature effects of the EXAFS Debye−Waller factor. The normalized XANES data from 8307 to 8399 eV were collected in a matrix, and singular value decomposition was used to determine the eigenvalues and eigenvectors.[56] To determine the number of principal components, the data were reconstructed with either two or three components and the residuals were plotted, following the method of Wang et al.[57] Ideally, pure phases would be selected for linear combination fitting to determine the mixing fractions of species as a function of temperature. However, using room-temperature reference spectra is not appropriate due to small changes in the XANES spectra at higher temperature. Therefore, iterative key set factor analysis (IKSFA[56]) was used to determine which of the XANES data sets were the most fundamental (i.e., best represent the entire data set through a linear combination of these data sets) and to select the intermediate spectra used for linear combination fitting of the data. IKSFA has been previously described in the literature for examining the intermediate state of Cu-ZSM-5 under reaction conditions.[58] For calculation of R-space EXAFS data, a k range of 2 to 13 and a k weight of 2 was used for the Fourier transform.

4. RESULTS

4.1. Structural and Morphological Properties of Ni/ZnO after Calcination. XRD patterns of Ni/ZnO and Ni/SiO_2 after calcination are shown in Figure 1. After oxygen treatment (calcination in air at 450 °C for 4 h), the only phases observable with XRD are NiO (JCPDS card no. 47-1049, NaCl structure) and ZnO (JCPDS card no. 36-1451, wurtzite structure) for the Ni/ZnO catalysts. A high-resolution scan of the region from 39 to 46° 2θ is shown in Figure 1, and complete scans are shown in Figure S1 of the Supporting Information. The intensity of the primary (200) reflection for NiO at 43.3° 2θ increases with increasing Ni weight loading for the series of Ni/ZnO catalysts. In comparison to Ni/SiO_2, Ni/ZnO displays NiO (200) reflections that are shifted to lower angles, indicating an expansion in lattice parameter and inclusion of Zn^{II} into the crystal lattice. Lattice parameters determined from Rietveld refinement of the XRD data are shown in Table 1. The extent of Zn^{II} substitution in the NiO lattice can be calculated from the NiO lattice parameter using the known lattice parameters of pure NiO (4.178 Å) and $Ni_{0.7}Zn_{0.3}O$ (4.211 Å) and a linear relationship between Zn content and lattice parameter, as demonstrated by Gaskell et al.[59,60] The Zn content ranges from 15 to 16% in the Ni/ZnO catalysts, well below the solubility limit of 32% in bulk NiO.[59] The insensitivity of Zn content with Ni loading is a result of having an infinite source of ZnO, leading to a similar crystal structure for NiO in each case. Crystallite sizes for NiO and ZnO were determined using the Scherrer formula and are displayed in Table 1. As expected, the NiO crystallite size increases with weight loading, from 21 nm (2 wt %) to 31 nm (10 wt %). Interestingly, the ZnO crystallite size also increases

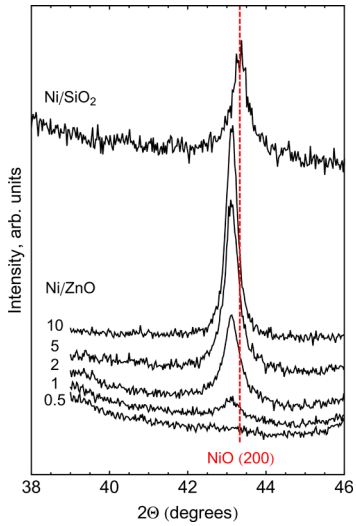

Figure 1. Powder X-ray diffraction of Ni/SiO_2 and Ni/ZnO catalysts after calcination at 450 °C. The weight loadings of the Ni/ZnO catalysts (0.5, 1, 2, 5, or 10 wt %) are indicated next to each diffractogram. The dotted line indicates the position of the (200) reflection for pure NiO. Complete PXRD patterns are shown in Figure S1 of the Supporting Information.

Table 1. Results from Powder X-ray Diffraction of Catalysts after Calcination

sample	Ni (wt %)	NiO a (Å)[a]	Zn in NiO (%)[b]	crystallite size (nm)[c] NiO	crystallite size (nm)[c] ZnO	BET surface area (m^2/g)
ZnO	0				14	40.8
Ni/ZnO	0.5	*d*	*d*	*d*	17	25.5
	1	*d*	*d*	*d*	20	22.7
	2	4.194 ± 0.001	15 ± 2	21	28	17.5
	5	4.194 ± 0.001	15 ± 2	26	39	15.9
	10	4.195 ± 0.001	16 ± 2	31	56	13.3
Ni/SiO_2	2	4.174 ± 0.001		20		278

[a]Determined from Rietveld refinement of the complete powder XRD data. [b]Calculated from the NiO lattice parameter on the basis of lattice parameters of pure NiO (4.178 Å) and $Ni_{0.7}Zn_{0.3}O$ (4.211 Å) and a linear relationship between Zn content and lattice parameter.[59,60] [c]Calculated from the fwhm of primary reflection using the Scherrer equation. [d]Not determined due to the low concentration of Ni in the sample.

DOI: 10.1021/acscatal.5b00627
ACS Catal. 2015, 5, 3304−3315

monotonically with Ni loading, suggesting that Ni facilitates the growth of ZnO. We hypothesize that as the concentration of Ni increases, the propensity for Zn^{II} diffusion also increases due to its ability to substitute for Ni^{II} in the crystal lattice of adjacent NiO NPs. An increased propensity for Zn^{II} diffusion would explain the observed ZnO size increase with Ni loading. BET surface areas (Table 1) also decrease monotonically with Ni loading, consistent with the analysis of crystallite size.

Low-magnification TEM of 2 wt % Ni/ZnO after calcination at 450 °C (Figure 2A) shows the polydisperse particle sizes of ZnO ranging from ∼10 to ∼100 nm. Differentiation between NiO and ZnO in TEM on the basis of contrast alone proves difficult due to the similar atomic numbers of Ni (28) and Zn (30). Figure 2B is a representative HRTEM image of the sample, with the fast Fourier transforms (FFTs) of a ZnO particle and NiO particle shown in Figure 2C,D, respectively.

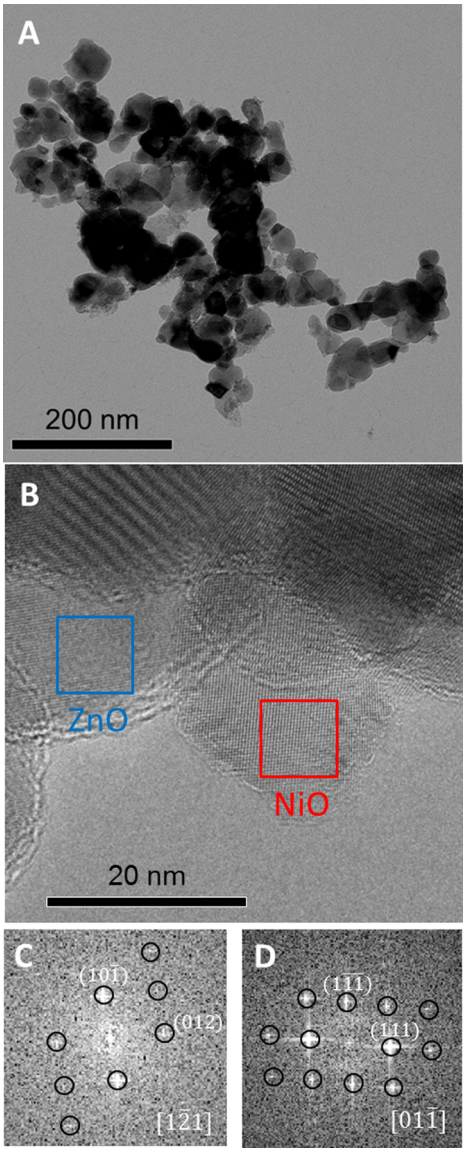

Figure 2. (A) Low-magnification transmission electron microscopy image of 2 wt % Ni/ZnO. (B) HRTEM image of 2 wt % Ni/ZnO. Corresponding FFT of (C) ZnO support and (D) NiO nanoparticle of 2 wt % Ni/ZnO after calcination at 450 °C. The ZnO particle is viewed from the [1$\bar{2}$1] zone axis, while the NiO particle is viewed from the [01$\bar{1}$] zone axis.

The zone axes of the ZnO and NiO particles are [1$\bar{2}$1] and [01$\bar{1}$], respectively. No species other than ZnO and NiO were observed in the HRTEM images. Electron energy loss spectroscopy (EELS) was also performed in STEM mode, and concentration maps of Ni and Zn were calculated from integration of the Ni and Zn edges, respectively. Representative elemental maps are shown in Figure S2A,B of the Supporting Information. The elemental maps illustrate the doping of Zn^{II} in the NiO NPs, supporting the results from XRD. Line scans across the NiO NPs show that Zn^{II} is evenly distributed throughout the NiO particles.

4.2. In Situ X-ray Absorption Spectroscopy. Structural changes during the reduction of Ni/ZnO were monitored by in situ X-ray absorption spectroscopy (XAS) during temperature-programmed reduction (TPR). Figure 3 shows the evolution of

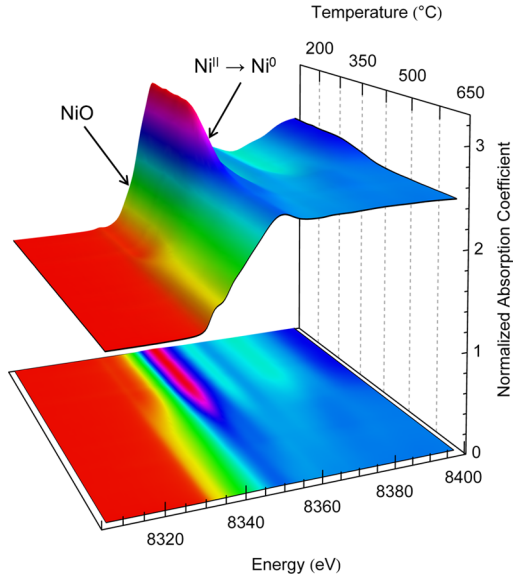

Figure 3. Ni K-edge XANES showing the temperature evolution of the in situ reduction of 2 wt % Ni/ZnO at a ramp rate of 1.3 °C/min and a 50 mL/min flow of 5% H_2/He. Ni is reduced from Ni^{II} to Ni^0 at ∼350 °C, as evidenced by a decrease in the height of the edge and a shift in energy of the onset of absorption.

the Ni K-edge XANES of 2 wt % Ni/ZnO from 200 to 650 °C. The spectra from 200 to 300 °C are consistent with NiO. When a temperature of 350 °C is reached, there is a decrease in the height of the white line peak which corresponds to the transition from Ni^{II} to Ni^0. Correspondingly, there is a shift in the onset of absorption (edge position) to lower energies which is also consistent with the reduction of NiO.

To determine the number of species present during reduction, it is helpful to examine the XANES scans overlaid in a two-dimensional image (Figure 4A). In this figure, there is no clear set of isosbestic points (the points at which all scans intersect). However, the XANES scans recorded from 102 to 507 °C (Figure 4B) display a series of isosbestic points. Spectra recorded at temperatures greater than 507 °C (Figure 4C) do not intersect the isosbestic points in Figure 4B; instead, these spectra exhibit a new set of isosbestic points. Figure 4B demonstrates that only two primary species are present up to ∼500 °C. The spectrum recorded at 102 °C is identical with that of NiO; thus, one of the primary species is NiO. The other primary species may be identified as α-NiZn, a Ni-rich substitutional solid solution with an FCC unit cell. The

DOI: 10.1021/acscatal.5b00627
ACS Catal. 2015, 5, 3304−3315

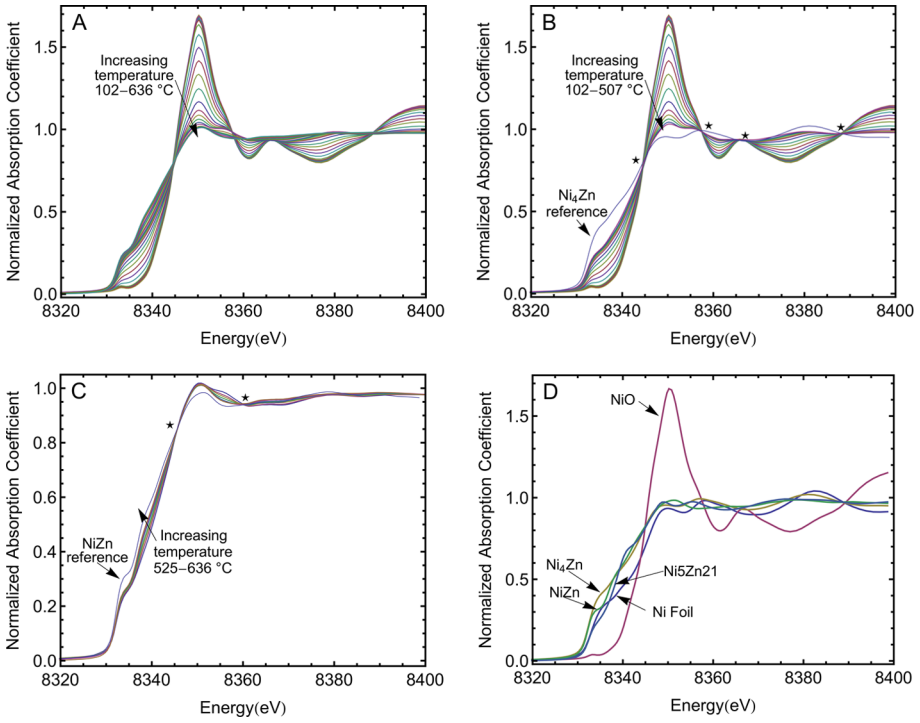

Figure 4. (A) Normalized Ni K-edge XANES spectra for the temperature-programmed reduction of 2 wt % Ni/ZnO at a ramp rate of 1.3 °C/min under a 50 mL/min flow of 5% H_2/He. (B) Subset of XANES spectra from 102 to 507 °C shown along with the Ni_4Zn reference spectrum. (C) Subset of XANES spectra from 525 to 636 °C shown along with the NiZn reference spectrum. (D) Reference XANES spectra for Ni foil, bulk Ni_4Zn, bulk NiZn, bulk Ni_5Zn_{21}, and NiO. In (B) and (C), asterisks indicate the position of isosbestic points.

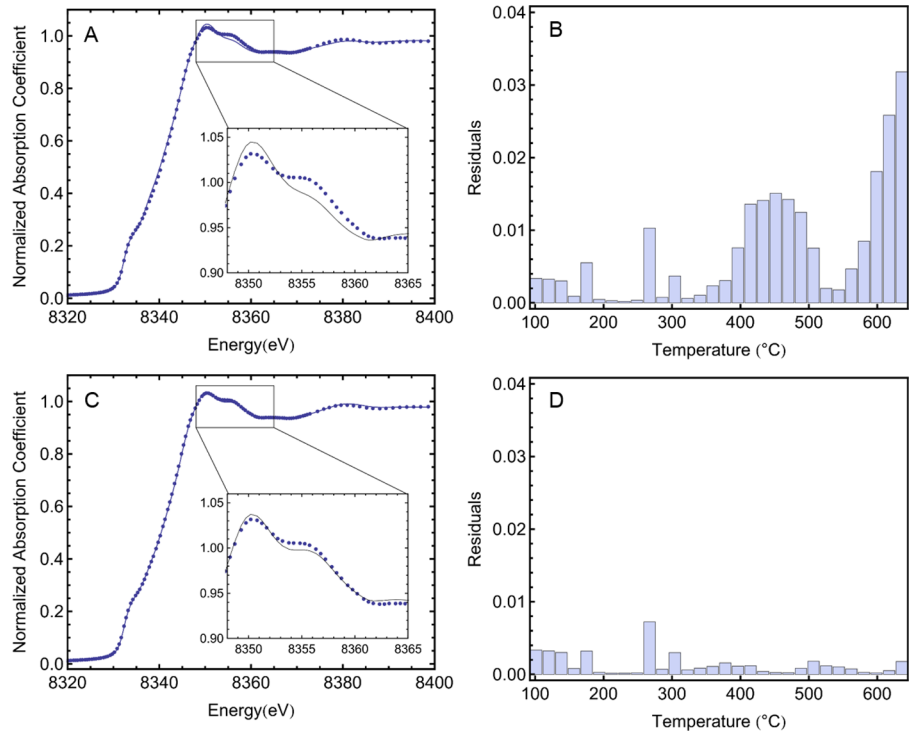

Figure 5. Principal component analysis of the Ni K-edge XANES spectra for the temperature-programmed reduction of 2 wt % Ni/ZnO at a ramp rate of 1.3 °C/min under a 50 mL/min flow of 5% H_2/He: (A) representative spectrum (dots) superimposed with the linear combination fitting of two principal components (solid line); (B) residual plot produced from the two-component fit to the data; (C) representative spectrum (dots) superimposed with the linear combination fitting of three principal components (solid line); (D) residual plot produced from the three-component fit to the data.

spectrum for the Ni_4Zn (α-NiZn) reference compound is plotted in Figure 4B along with the in situ data. Ni_4Zn intersects at each of the isosbestic points formed by the data. Thus, it is clear that there is a direct transition from NiO to α-

DOI: 10.1021/acscatal.5b00627
ACS Catal. 2015, 5, 3304−3315

NiZn with a Zn concentration near 20 mol % (that of Ni_4Zn). In addition to Ni_4Zn, the spectra in Figure 4B were overlaid with the spectra for pure Ni foil, intermetallic β_1-NiZn, and intermetallic Ni_5Zn_{21} (shown in Figure 4D), but these spectra do not intersect the isosbestic points. This set of XANES reference materials encompasses all of the known Ni−Zn phases that form below 700 °C and have Zn contents of less than 90%.[61] It is likely that α-NiZn forms at the interface of the NiO and ZnO as the reduction takes place. The spectra recorded from 525 to 636 °C demonstrate that a second phase change takes place (Figure 4C). These data show two isosbestic points that are different from the scans from 102 to 507 °C and intersect with the intermetallic β_1-NiZn reference spectrum. Thus, the Ni phase undergoes a second transition from α-NiZn to β_1-NiZn starting at ∼525 °C. We rule out the possibility of formation of the high-temperature cubic β-NiZn phase, since the temperature required for formation is ∼700 °C on the basis of the published Ni−Zn bulk phase diagram.[61] The spectrum for Ni_5Zn_{21} was also compared with the data in Figure 4C, and it does not intersect at the isosbestic points. The analysis of the isosbestic points of the temperature-dependent XANES data shows that three primary Ni-based phases are present, with NiO transforming first to α-NiZn followed by a transformation to β_1-NiZn.

We performed principal component analysis (PCA) of the XANES data following the methods of Wang et al.[57] to provide another measure of the number of phases present in the XANES data. The XANES spectra $\mu(E)$ values in the energy range 8307−8399 eV and temperature range 102−636 °C were used for calculation of the eigenvectors of the data set. Subsequently, the data were fit with a linear combination of the two principal components (Figure 5A). The data and the two-component fit display a significant misfit in the region 8350−8360 eV, indicating that two principal components do not adequately reproduce the data. The fit residuals (Figure 5B) show peaks at 470 and 630 °C which are consistent with phase transformations at these temperatures. Using three principal components to reproduce the data (Figure 5C) results in an improved fit and residuals (Figure 5D) within the statistical noise in the data.

Principal component analysis and the analysis of isosbestic points are both consistent with three phases present during the in situ reduction: NiO, α-NiZn, and β_1-NiZn. We used linear combination fitting of the XANES spectra to determine the percentage of each phase present during reduction. Since the data have been collected at different temperatures, it is inappropriate to use the room-temperature reference spectra in Figure 4D for linear combination fitting. Instead, we used IKSFA[56] to determine which of the XANES spectra were most fundamental (i.e., the spectra that best represent the entire data set through a linear combination of these spectra) and fit the rest of the data with a linear combination of these spectra. IKSFA resulted in an intermediate component at a temperature of 507 °C, which we assign to α-NiZn. The XANES data were then fit with a linear combination of the first spectrum, the spectrum at 507 °C, and the last spectrum to give the results shown in Figure 6. Since IKSFA was used to determine the XANES spectra used for linear combination fitting (and no true temperature-dependent reference materials were used), the mole fractions of α-NiZn and β_1-NiZn are, by definition, 1 at 507 and 636 °C, respectively. However, this is an artifact of the data analysis procedure and the sample may actually be composed of multiple phases at 507 and 636 °C. Additionally,

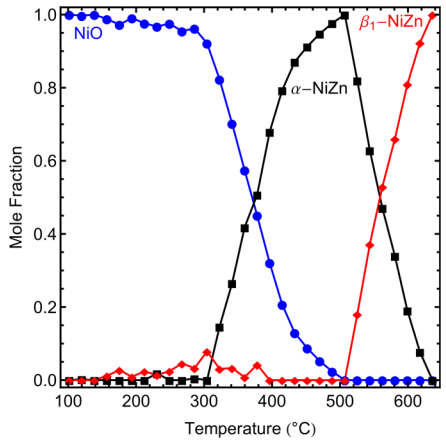

Figure 6. Phase composition of each XANES spectra during the temperature-programmed reduction of 2 wt % Ni/ZnO as determined from factor analysis using a three-component fit.

the transitions are probably smoother, as the abrupt changes from one composition to another may also be a result of the data analysis procedure. However, Figure 6 still provides a qualitative assessment of the stepwise transformation of NiO to α-NiZn and finally β_1-NiZn.

The temperature evolution of the Fourier transform *R*-space EXAFS is shown in Figure 7. No phase corrections in the

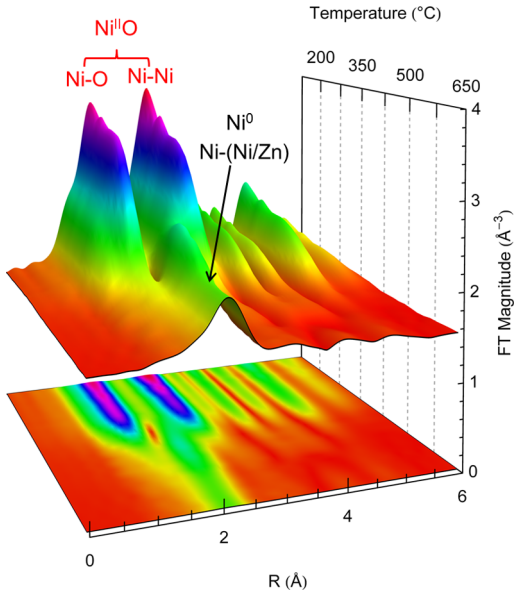

Figure 7. Fourier transform Ni *K*-edge *R*-space EXAFS spectra of the in situ reduction of 2 wt % Ni/ZnO. Labels indicate the presence of two peaks which represent Ni−O and Ni−Ni scattering of NiO at low temperatures and a single peak characteristic of Ni−M (M = Ni, Zn) scattering at high temperatures.

EXAFS data have been performed. The peak at low temperatures at 1.6 Å corresponds to contributions from the nearest oxygen neighbor of NiO. The low-temperature peak at 2.5 Å corresponds to contributions from the nearest Ni atom in NiO. As the reduction proceeds, these two primary peaks disappear and are replaced by a single peak centered at 2.2 Å, characteristic of Ni or Zn nearest neighbors. The EXAFS results are consistent with the results of XANES. Quantitative analysis of the EXAFS was not performed due to the increase in EXAFS

DOI: 10.1021/acscatal.5b00627
ACS Catal. 2015, 5, 3304−3315

Debye–Waller factor at high temperatures, which significantly reduces the magnitude of EXAFS oscillations and makes differentiation between structures difficult. Additionally, differentiation between Ni and Zn backscatterers proves difficult because they have similar EXAFS phase shifts and backscattering amplitudes as a result of being separated by only one element on the periodic table.

4.3. Temperature-Programmed Reduction. Figure 8 shows the hydrogen consumption during the temperature-programmed reduction (TPR) of the 2 wt % Ni/ZnO catalyst. The temperature ramp rate for this experiment is 10 °C/min in comparison to the 1.3 °C/min ramp rate of the in situ XAS experiment. The data exhibit two peaks centered at 400 and 550 °C, respectively. The data were fit with two Gaussian-shaped peaks, which we attribute to the reduction of two different species. On the basis of the results obtained from the XANES data, we assign the 400 °C peak to the reduction of NiO, since this temperature is consistent with the temperature at which NiO transformed to α-NiZn (as shown in Figure 6). Also on the basis of the results shown in Figure 6, the only reducible species present above 500 °C is ZnO. Therefore, we assign the second peak centered at 550 °C to the reduction of ZnO. The amounts of hydrogen consumed in the first and second peaks are 1.08 and 0.97 equiv of Ni in the sample, respectively. These results suggest that equal amounts of NiO and ZnO are reduced, which is consistent with the stoichiometry necessary for the formation of intermetallic NiZn.

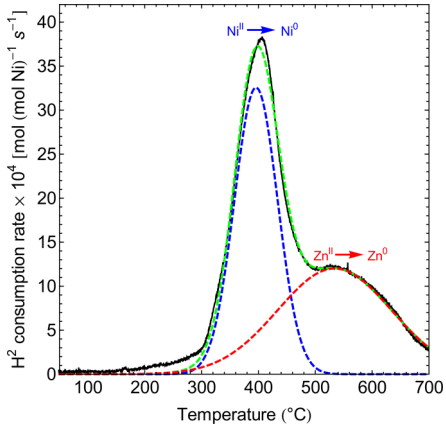

Figure 8. Ex situ temperature-programmed reduction of 2 wt % Ni/ZnO (10 °C/min, 50 mL/min 3.88% H_2/Ar). Data (solid black line) were fit (dotted green line) with two Gaussian-shaped peaks (dotted blue and dotted red lines). The first and second peaks are assigned to the reduction of Ni (1.08 equiv of Ni) and Zn (0.97 equiv of Ni), respectively.

4.4. Ex Situ Characterization of Ni/ZnO after Reduction. A low-magnification TEM image of the 2 wt % Ni/ZnO catalyst after reduction is presented in Figure 9A. In contrast to the TEM images after calcination, the metallic nanoparticles now show contrast with respect to the ZnO support. In Figure 9B–D, HRTEM images of metallic nanoparticles adsorbed to the ZnO support are shown. FFTs of the metallic nanoparticles (boxed areas) are shown in the inset of each HRTEM image. By comparison of the experimental distances and angles of the vectors in the FFT to those of possible structures, including ZnO, Ni, α-NiZn, β_1-NiZn, and NiO, the FFT in Figure 9B was indexed to the [100] zone axis of β_1-NiZn. The vector lengths

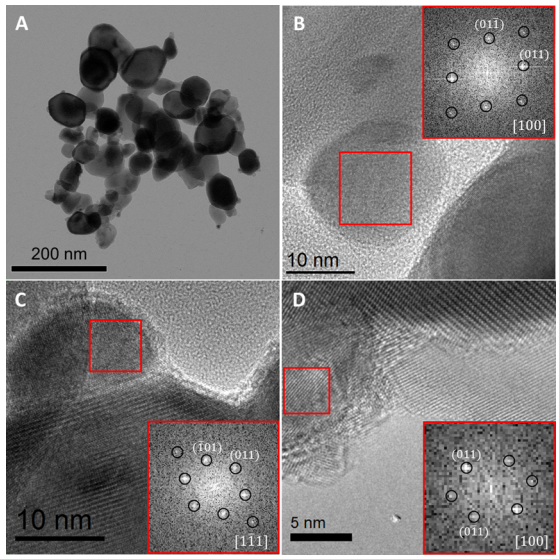

Figure 9. Transmission electron microscopy images of 2 wt % Ni/ZnO reduced at 600 °C: (A) low magnification TEM image, (B–D) HRTEM images of β_1-NiZn nanoparticles. The insets show indexed FFTs of boxed areas. The β_1-NiZn particles are viewed from the [100], [1$\bar{1}$1], and [100] zone axes in images B–D, respectively.

of and the angle between the (01$\bar{1}$) and (011) vectors are 2.03 Å and 77.5°, respectively. This is comparable to the expected vector lengths and angle for β_1-NiZn (a = 2.751 Å, c = 3.181 Å) of 2.08 Å and 81.7°, respectively. A calculated FFT of a distorted β_1-NiZn unit cell with a small elongation in the c direction and compression in the a and b directions, with lattice parameters a = 2.61 Å and c = 3.24 Å, matches the experimental FFT shown in Figure 9B. The FFT in Figure 9C can also be indexed to β_1-NiZn, where this particle is oriented along the [1$\bar{1}$1] zone axis. The vector lengths of and angle between the ($\bar{1}$01) and (011) vectors are 2.03 Å and 66°, respectively, in comparison to the expected vector lengths and angle for β_1-NiZn of 2.08 Å and 65°, respectively. Similar to the structure of the particle in Figure 9B, the structure of the particle in Figure 9C matches more closely to a distorted β_1-NiZn unit cell. The vector lengths of and angle between the (011) and (0$\bar{1}$1) vectors of the particle in Figure 9D (2.04 Å and 96°, respectively) also have slight deviations compared to those of the β_1-NiZn (2.08 Å and 98°, respectively) and would match a distorted β_1-NiZn unit cell.

The three examples of β_1-NiZn shown in Figure 9 demonstrate the presence of β_1-NiZn, but they neither prove that the entire catalyst is homogeneous nor disprove the presence of other Ni–Zn phases such as α-NiZn. However, the HRTEM results do provide a qualitative assessment of the composition of the Ni–Zn NPs and they support the results from the in situ XANES experiments. A portion of the Ni–Zn NPs appeared to be encased in an amorphous oxide shell, with an example being shown in Figure 9C. Other NPs, such as the particle shown in Figure 9D, show lattice planes that extend to the surface. It is possible that the oxide shell formed during a short (~1 min) exposure of the sample to air during loading into the TEM.

The results of ex situ XRD after reduction are shown in Figure 10 and Table 2, with the complete patterns shown in Figure S3 of the Supporting Information. In addition to 2 wt % Ni/ZnO, we also examined 0.5, 1.0, 5.0, and 10 wt % Ni/ZnO catalysts. After reduction (3.88% H_2 in Ar, 10 °C/min to 600

DOI: 10.1021/acscatal.5b00627
ACS Catal. 2015, 5, 3304–3315

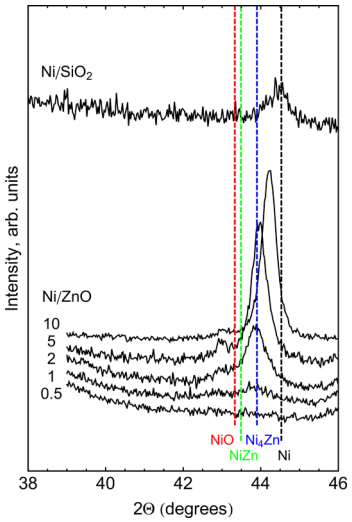

Figure 10. Ex situ powder X-ray diffraction of Ni/SiO_2 and Ni/ZnO catalysts after reduction to 600 °C. The dotted lines indicate the reflections for NiO (200), β_1-NiZn (101), Ni_4Zn (111), and Ni (111).

Table 2. Results from ex Situ Powder X-ray Diffraction of Catalysts after Temperature-Programmed Reduction to 600 °C

sample	amt of Ni (wt %)	position of primary reflection (deg 2θ)	crystallite size (nm)[a] Ni	crystallite size (nm)[a] ZnO
ZnO	0			19
Ni/ZnO	0.5	*b*	*b*	20
	1	43.82	11	22
	2	43.85	15	29
	5	43.97	21	42
	10	44.24	23	59
Ni/SiO_2	2		20	

[a]Calculated from fwhm of primary reflection using the Scherrer equation. [b]Not determined due to the low concentration of Ni in the sample.

°C), each catalyst displays a primary reflection that has shifted to lower angles and is characteristic of a larger unit cell and thus a Ni−Zn structure. The shift to lower angles is more pronounced in the low weight loading samples (0.5, 1, and 2 wt %) than the high weight loading samples (5 and 10 wt %). This effect can be rationalized in terms of the barrier for Zn^{II} reduction and subsequent diffusion into the Ni NPs. The high weight loading samples contain larger Ni crystallites and, correspondingly, low surface area to volume ratios that inhibit Zn incorporation. A quantitative analysis of the ex situ XRD data is not presented because of the inability of these data to describe the physical states of the catalysts under reduction or reaction conditions. The Ni/ZnO peaks can be assigned to the (111) reflection of a face-centered cubic α-NiZn alloy with an expanded lattice parameter in comparison to pure Ni metal (e.g., Ni_4Zn). However, since the catalysts were exposed to air prior to the ex situ XRD analysis, it is likely that the observed reflection for α-NiZn is a product of β_1-NiZn decomposition. The decomposition behavior of β_1-NiZn to α-NiZn and ZnO has previously been demonstrated in the literature by Friedrich et al.[44]

In addition to laboratory XRD, we employed synchrotron XRD and pair distribution function (PDF) analysis of the catalysts. The radial distribution functions $G(r)$ are in shown in Figure S4 of the Supporting Information. Since the radial distribution functions are not element specific, the ZnO was fitted and subtracted from each spectrum to gain insight into the nature of the Ni phase. The results from fitting the NiO phase in each of the calcined samples are shown in Table S1 of the Supporting Information. The data provided results similar to those of the laboratory XRD analysis.

4.5. Selectivity for Acetylene Semihydrogenation in the Presence of Ethylene. The selectivity for acetylene semihydrogenation in the presence of excess ethylene was measured in a batch reactor following the method we previously used.[29] The catalytic behavior of 2 wt % Ni/ZnO was examined after three different reduction temperatures (400, 500, and 600 °C) and compared with 2 wt % Ni/SiO_2 reduced at 450 °C. The reactions were carried out at a temperature of 160 °C with a reactant mixture consisting of 5 Torr of $^{13}C_2H_2$, 26 Torr of H_2, and 53 Torr of $^{12}C_2H_4$. Isotopic labeling allows for the direct determination of ethylene selectivity.[29]

The partial pressures of $^{13}C_2H_2$, $^{13}C_2H_4$, $^{13}C_2H_6$, and $^{12}C_2H_6$ as a function of time are shown in Figure 11. Time 0 is defined as the time at which the reactor reached 160 °C. The reactor took ∼10 min to heat from room temperature to 160 °C; thus, there is an inherent offset in the *x*-axis time values due to the inability to heat the reactor instantaneously. The 2 wt % Ni/ZnO catalyst reduced at 600 °C (Figure 11A) has a low propensity for overhydrogenation, producing very little $^{13}C_2H_6$ and $^{12}C_2H_6$. Additionally, the same catalyst produces 0.9 Torr of $^{13}C_2H_4$ at full conversion of acetylene, which had a starting pressure of 5.3 Torr, which amounts to only 17% conversion of the acetylene to ethylene. Ni/SiO_2 (Figure 11B), conversely, converts 40% of the starting acetylene to ethylene and produces substantial amounts of $^{12}C_2H_6$ after all of the acetylene has reacted. The 2 wt % Ni/ZnO catalyst reduced at 400 and 500 °C showed catalytic behavior similar to that for the 600 °C reduction temperature, with the results shown in Table 3 (time-dependent behavior for these materials is shown in Figure S5 of the Supporting Information). The reduction temperature of Ni/ZnO (400, 500, or 600 °C) does not appear to be critical to selectivity. In comparison to Ni/SiO_2, Ni/ZnO exhibits a reduction in turnover frequency and a significant reduction in ethylene formation. The reduction in ethylene formation is a result of an increase in oligomerization on the ZnO-supported catalysts. In fact, all of the Ni/ZnO catalysts convert ∼80% of the initial acetylene to oligomers, on the basis of a carbon balance.

Pure ZnO recorded a measurable conversion of acetylene (Figure S5 of the Supporting Information), oligomerizing acetylene to form 99% higher molecular weight products, with only 1% of the acetylene converted to ethylene. The rate of acetylene removal was 2−5 times slower (on a per gram basis) than that of the Ni/ZnO catalysts. Thus, it is clear that it is important to consider the effect of ZnO when evaluating the selectivity of Ni/ZnO catalysts. However, since ZnO converts acetylene to oligomers (instead of hydrogenation products), it is imperative that an absolute measure of ethylene selectivity is used for evaluation. Conversely, previous studies[28,31] have measured ethane concentration alone as a measure of ethylene selectivity, where catalysts that produced low concentrations of ethane were regarded as selective catalysts. However, by this

DOI: 10.1021/acscatal.5b00627
ACS Catal. 2015, 5, 3304−3315

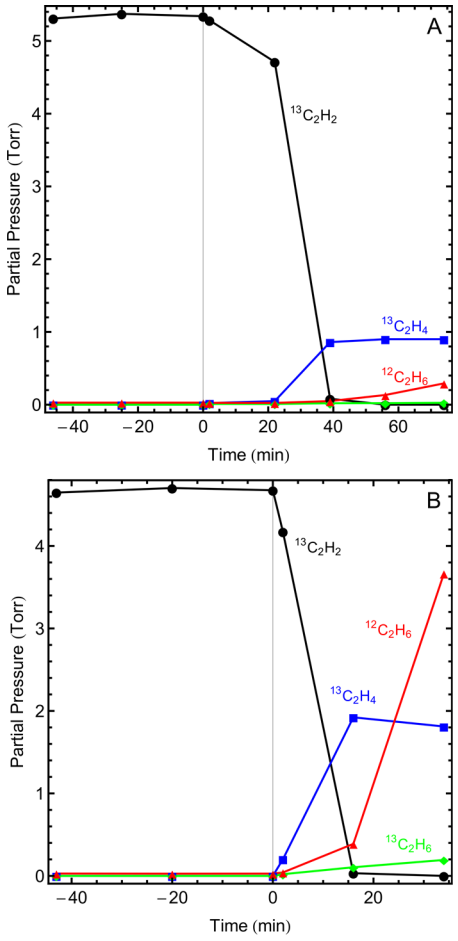

Figure 11. Partial pressures of $^{13}C_2H_2$ (black), $^{13}C_2H_4$ (blue), $^{12}C_2H_6$ (red), and $^{13}C_2H_6$ (green) as a function of time during the catalytic hydrogenation of acetylene in the presence of ethylene in a batch reactor at 160 °C for (A) 200 mg of 2 wt % Ni/ZnO reduced at 600 °C and (B) 15 mg of 2 wt % Ni/SiO_2 reduced at 450 °C. Initial partial pressures of $^{13}C_2H_2$, H_2, and $^{12}C_2H_4$ were ~5, 26, and 53 Torr, respectively. The solid line indicates the time at which the reactor reached 160 °C.

Table 3. Catalytic Activity and Selectivity for the Semihydrogenation of Acetylene in the Presence of Ethylene in a Batch Reactor at 160 °C[a]

catalyst	reduction temp (°C)	rate (mol of C_2H_2/((g of cat.) s))	TOF (s^{-1})	$^{13}C_2H_4$ selectivity[b]
Ni/SiO_2	450	5.9×10^{-7}	3.5×10^{-2}	40
Ni/ZnO	400	8.9×10^{-9}	5.5×10^{-4}	20
	500	2.5×10^{-8}	1.6×10^{-3}	18
	600	2.1×10^{-8}	1.3×10^{-3}	17
ZnO	500	5.2×10^{-9}	6.3×10^{-6}	1

[a]Initial partial pressures of $^{13}C_2H_2$, H_2, and $^{12}C_2H_4$ were ~5, 26, and 53 Torr, respectively. [b]$^{13}C_2H_4$ selectivity is defined as the final partial pressure of $^{13}C_2H_4$ divided by the initial partial pressure of $^{13}C_2H_2$.

definition, ZnO would be considered a selective catalyst, when in reality it produces very little ethylene.

To gain additional insight into the catalytic behavior of the catalysts, we measured the rate of H−D exchange on Ni/SiO_2, Ni/ZnO reduced at 500 °C, and ZnO. The temperature dependence of the H−D exchange is shown in Figure 12. Ni/SiO_2 has the highest rate of H−D exchange, reaching near HD equilibrium at ~100 °C. For Ni/ZnO and ZnO, temperatures

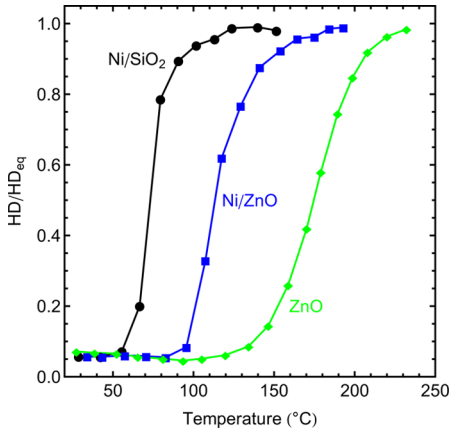

Figure 12. Temperature dependence of H−D exchange with equal H_2 and D_2 flow rates (10 mL/min).

of 150 and 200 °C, respectively, are required for similar levels of HD formation.

5. DISCUSSION

Our results demonstrate that the calcination of nickel nitrate on a ZnO nanoparticle support leads to Zn-doped NiO NPs with a formula of ca. $Ni_{0.85}ZnO_{0.15}$ and the rock salt crystal structure. The XANES analysis of the in situ reduction shows a direct transition from the Zn-doped NiO NPs to Ni_xZn_{1-x}, a Ni-rich substitutional solid solution with a face centered cubic structure. Thus, it is reasonable for us to conclude that the Zn present in the Ni NPs during the initial phases of the reduction was incorporated during the calcination step. At ~550 °C, Ni_xZn_{1-x} transformed to intermetallic β_1-NiZn, with the fraction of β_1-NiZn in the sample increasing with temperature. In contrast to the initial stages of reduction, the reduction of ZnO and diffusion of Zn at high temperatures is necessary for the increased molar ratio of Zn in the NPs and the formation of intermetallic NiZn. These results are summarized in Scheme 1.

It is important to note that the NiZn phases are not stable when exposed to air. Ex situ XANES spectra at the Ni K-edge of reduced 2 wt % Ni/ZnO after exposure to air (not shown) demonstrated an increase in the white line height, indicative of the oxidation of Ni. The oxidation of Zn after exposure to air could not be probed by XANES due to the excess ZnO in the sample. However, it has been shown previously that ZnO is a decomposition product of intermetallic NiZn after exposure to oxidizing conditions.[44] In addition, we found no evidence for the formation of Ni−Zn compounds with higher Zn content such as Ni_5Zn_{21}, presumably due to the high vapor pressure of Zn at the temperatures required to reduce a sufficient amount of Zn to form Ni_5Zn_{21}.

In our previous work, we examined the selectivity for acetylene semihydrogenation on bulk intermetallic Ni−Zn catalysts.[29] We found that a favorable increase in ethylene selectivity could be attributed to a reduced binding energy of acetylene on the catalyst surface, due to the incorporation of Zn into the crystal lattice. The reduced binding energy of acetylene combined with only a moderate change in H binding energy led to a reduced propensity for acetylene oligomerization and an increase in ethylene production. In this work, we find that the Ni/ZnO catalysts display a lower selectivity to ethylene production than Ni/SiO_2, which is in contrast to the case for the aforementioned bulk intermetallic Ni−Zn catalysts, which

DOI: 10.1021/acscatal.5b00627
ACS Catal. 2015, 5, 3304−3315

Scheme 1. Demonstration of the Progression of the Ni Phases during Reduction

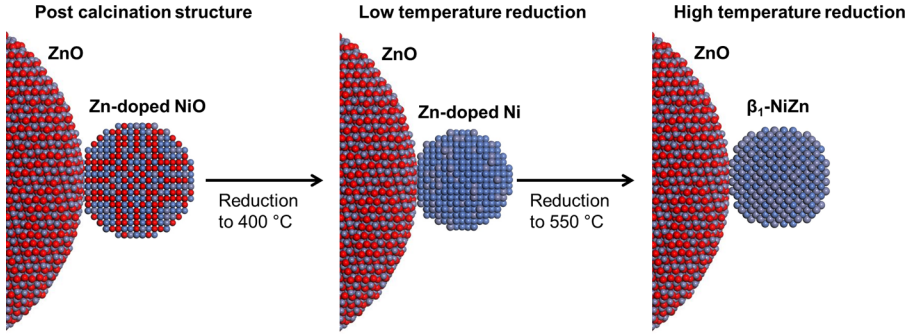

showed increasing ethylene selectivity with increasing Zn content.[29] Thus, from the results of our current study and from comparison with our previous study, it is clear that the ZnO support has a negative influence on ethylene selectivity. The benefit that β_1-NiZn provides in terms of ethylene selectivity is not sufficient to overcome the decrease in ethylene selectivity as a result of acetylene oligomerization on the ZnO support. The observed ethylene selectivities for the Ni/ZnO catalysts (17−20%) can be thought of as a linear combination of the intrinsic selectivities of β_1-NiZn and ZnO, with ZnO dominating acetylene removal. The similarity in catalytic selectivity of the three Ni/ZnO catalysts reduced at 400, 500, or 600 °C further substantiates the conclusion that ZnO is dominating the acetylene removal process. The XANES results show that the incorporation of Zn into the Ni phase increases with increasing temperature, while the catalytic selectivity results provide no indication that additional Zn content favors ethylene selectivity.

The H−D exchange experiments provide additional insight into the reason for the catalytic behavior of the Ni/ZnO materials. The ability of Ni/ZnO to dissociate hydrogen is severely reduced in comparison to Ni/SiO_2, with Ni/ZnO not reaching H−D equilibrium until the temperature is nearly 50 °C higher than that for Ni/SiO_2. Conversely, the calculated adsorption energies of H on Ni (111) and β_1-NiZn (101) are 0.46 and 0.47 eV, respectively.[29] Therefore, the difference in the abilities of Ni/ZnO to dissociate hydrogen in comparison to Ni/SiO_2 can be attributed to the presence of ZnO. The presence of ZnO leads to an inability of the catalyst to dissociate hydrogen, thereby favoring acetylene oligomerization over acetylene hydrogenation.

6. CONCLUSIONS

Through a combination of in situ XANES measurements and ex situ TEM, we have monitored the phase transformations that Ni/ZnO catalysts undergo during reduction. Zn-doped NiO NPs are reduced to form a Ni-rich solid solution (α-NiZn) at 400 °C and are finally converted to intermetallic β_1-NiZn at 550 °C. Catalytic measurements show that, independent of reduction temperature, Ni/ZnO is not a selective catalyst for acetylene semihydrogenation in the presence of excess ethylene as a result of oligomerization occurring on the ZnO support. This work highlights that the extrapolation from DFT or bulk materials to supported catalysts is often broken due to the complexities that arise in real materials. Further studies on bimetallic Ni-based hydrogenation catalysts should strive to create well-defined intermetallic structures supported on inert materials, minimizing undesired reaction pathways such as the oligomerization of acetylene.

■ ASSOCIATED CONTENT

Supporting Information

The following file is available free of charge on the ACS Publications website at DOI: 10.1021/acscatal.5b00627.

Complete PXRD patterns, HRTEM EELS images, synchrotron high-energy X-ray scattering and pair distribution function analysis, and catalytic data for the selective hydrogenation of acetylene (PDF)

■ AUTHOR INFORMATION

Corresponding Author

*R.M.R.: e-mail, rioux@engr.psu.edu; tel, (814) 867-2503.

Notes

The authors declare no competing financial interest.

■ ACKNOWLEDGMENTS

Acknowledgement is made to the donors of The American Chemical Society Petroleum Research Fund (ACS PRF #50-794-DN15) for support of this research. Beamline X19A is supported, in part, by US DOE Grant No. DE-FG02-05ER15688. The authors thank the Synchrotron Catalysis Consortium (SCC) for use of in situ reactor equipment and Dr. Nebojsa Marinkovic for help with acquisition of the XAS data. This research used resources of the Advanced Photon Source, a U.S. Department of Energy (DOE) Office of Science User Facility operated for the DOE Office of Science by Argonne National Laboratory under Contract No. DE-AC02-06CH11357. The high-energy X-ray scattering data were collected at beamline 11-ID-B at the Advanced Photon Source, Argonne National Laboratory. C.S.S. acknowledges the National Science Foundation under Grant No. DGE1255832. Any opinions, findings, and conclusions, or recommendations expressed in this material are those of the author(s) and do not necessarily reflect the views of the National Science Foundation.

■ REFERENCES

(1) Borodziński, A.; Bond, G. C. *Catal. Rev.: Sci. Eng.* **2006**, *48*, 91−144.
(2) Schbib, N. S.; García, M. A.; Gígola, C. E.; Errazu, A. F. *Ind. Eng. Chem. Res.* **1996**, *35*, 1496−1505.
(3) Borodziński, A.; Cybulski, A. *Appl. Catal., A* **2000**, *198*, 51−66.
(4) Zhang, Q.; Li, J.; Liu, X.; Zhu, Q. *Appl. Catal., A* **2000**, *197*, 221−228.
(5) Zea, H.; Lester, K.; Datye, A. K.; Rightor, E.; Gulotty, R.; Waterman, W.; Smith, M. *Appl. Catal., A* **2005**, *282*, 237−245.
(6) Praserthdam, P.; Ngamsom, B.; Bogdanchikova, N.; Phatanasri, S.; Pramotthana, M. *Appl. Catal., A* **2002**, *230*, 41−51.

DOI: 10.1021/acscatal.5b00627
ACS Catal. 2015, 5, 3304−3315

(7) Panpranot, J.; Nakkararuang, L.; Ngamsom, B.; Praserthdam, P. *Catal. Lett.* **2005**, *103*, 53−58.
(8) Khan, N. A.; Shaikhutdinov, S.; Freund, H. J. *Catal. Lett.* **2006**, *108*, 159−164.
(9) Han, Y.; Peng, D.; Xu, Z.; Wan, H.; Zheng, S.; Zhu, D. *Chem. Commun. (Cambridge, U. K.)* **2013**, *49*, 8350−8352.
(10) González, S.; Neyman, K. M.; Shaikhutdinov, S.; Freund, H.-J.; Illas, F. *J. Phys. Chem. C* **2007**, *111*, 6852−6856.
(11) Borodziński, A.; Bond, G. C. *Catal. Rev.: Sci. Eng.* **2008**, *50*, 379−469.
(12) Bond, G. C.; Dowden, D. A.; Mackenzie, N. *Trans. Faraday Soc.* **1958**, *54*, 1537−1546.
(13) Frevel, L. K.; Kressley, L. J. U.S. Patent 2,802,889, August 13, 1957.
(14) Armbrüster, M.; Kovnir, K.; Behrens, M.; Teschner, D.; Grin, Y.; Schlögl, R. *J. Am. Chem. Soc.* **2010**, *132*, 14745−14747.
(15) Kovnir, K.; Armbrüster, M.; Teschner, D.; Venkov, T. V.; Szentmiklósi, L.; Jentoft, F. C.; Knop-Gericke, A.; Grin, Y.; Schlögl, R. *Surf. Sci.* **2009**, *603*, 1784−1792.
(16) Osswald, J.; Giedigkeit, R.; Jentoft, R. E.; Armbrüster, M.; Girgsdies, F.; Kovnir, K.; Ressler, T.; Grin, Y.; Schlögl, R. *J. Catal.* **2008**, *258*, 210−218.
(17) Ota, A.; Armbrüster, M.; Behrens, M.; Rosenthal, D.; Friedrich, M.; Kasatkin, I.; Girgsdies, F.; Zhang, W.; Wagner, R.; Schlögl, R. *J. Phys. Chem. C* **2010**, *115*, 1368−1374.
(18) Osswald, J.; Kovnir, K.; Armbrüster, M.; Giedigkeit, R.; Jentoft, R. E.; Wild, U.; Grin, Y.; Schlögl, R. *J. Catal.* **2008**, *258*, 219−227.
(19) Armbrüster, M.; Kovnir, K.; Friedrich, M.; Teschner, D.; Wowsnick, G.; Hahne, M.; Gille, P.; Szentmiklósi, L.; Feuerbacher, M.; Heggen, M.; Girgsdies, F.; Rosenthal, D.; Schlögl, R.; Grin, Y. *Nat. Mater.* **2012**, *11*, 690−693.
(20) Bridier, B.; Lopez, N.; Perez-Ramirez, J. *Dalton Trans.* **2010**, *39*, 8412−8419.
(21) Bridier, B.; Pérez-Ramírez, J. *J. Am. Chem. Soc.* **2010**, *132*, 4321−4327.
(22) Bridier, B.; López, N.; Pérez-Ramírez, J. *J. Catal.* **2010**, *269*, 80−92.
(23) Abelló, S.; Verboekend, D.; Bridier, B.; Pérez-Ramírez, J. *J. Catal.* **2008**, *259*, 85−95.
(24) Boudjahem, A.-G.; Monteverdi, S.; Mercy, M.; Bettahar, M. M. *Appl. Catal., A* **2003**, *250*, 49−64.
(25) Peña, J. A.; Herguido, J.; Guimon, C.; Monzón, A.; Santamaría, J. *J. Catal.* **1996**, *159*, 313−322.
(26) Trimm, D. L.; Liu, I. O. Y.; Cant, N. W. *J. Mol. Catal. A: Chem.* **2008**, *288*, 63−74.
(27) Trimm, D. L.; Liu, I. O. Y.; Cant, N. W. *Appl. Catal., A* **2010**, *374*, 58−64.
(28) Studt, F.; Abild-Pedersen, F.; Bligaard, T.; Sørensen, R. Z.; Christensen, C. H.; Nørskov, J. K. *Science* **2008**, *320*, 1320−1322.
(29) Spanjers, C. S.; Held, J. T.; Jones, M. J.; Stanley, D. D.; Sim, R. S.; Janik, M. J.; Rioux, R. M. *J. Catal.* **2014**, *316*, 164−173.
(30) Batyrev, E. D.; van den Heuvel, J. C. *Phys. Chem. Chem. Phys.* **2011**, *13*, 13127−13134.
(31) Trimm, D. L.; Cant, N. W.; Liu, I. O. Y. *Catal. Today* **2011**, *178*, 181−186.
(32) Rives, V.; Labajos, F. M.; Trujillano, R.; Romeo, E.; Royo, C.; Monzón, A. *Appl. Clay Sci.* **1998**, *13*, 363−379.
(33) Rodríguez, J. C.; Marchi, A. J.; Borgna, A.; Monzón, A. *J. Catal.* **1997**, *171*, 268−278.
(34) Monzón, A.; Romeo, E.; Royo, C.; Trujillano, R.; Labajos, F. M.; Rives, V. *Appl. Catal., A* **1999**, *185*, 53−63.
(35) Jung, K.-D.; Joo, O.-S.; Han, S.-H. *Catal. Lett.* **2000**, *68*, 49−54.
(36) Conant, T.; Karim, A. M.; Lebarbier, V.; Wang, Y.; Girgsdies, F.; Schlögl, R.; Datye, A. *J. Catal.* **2008**, *257*, 64−70.
(37) Iwasa, N.; Takezawa, N. *Top. Catal.* **2003**, *22*, 215−224.
(38) Karim, A. M.; Conant, T.; Datye, A. K. *Phys. Chem. Chem. Phys.* **2008**, *10*, 5584−5590.
(39) Takezawa, N.; Iwasa, N. *Catal. Today* **1997**, *36*, 45−56.
(40) Iwasa, N.; Masuda, S.; Takezawa, N. *React. Kinet. Catal. Lett.* **1995**, *55*, 349−353.
(41) Ammari, F.; Lamotte, J.; Touroude, R. *J. Catal.* **2004**, *221*, 32−42.
(42) Consonni, M.; Jokic, D.; Yu Murzin, D.; Touroude, R. *J. Catal.* **1999**, *188*, 165−175.
(43) Loricera, C. V.; Castano, P.; Infantes-Molina, A.; Hita, I.; Gutierrez, A.; Arandes, J. M.; Fierro, J. L. G.; Pawelec, B. *Green Chem.* **2012**, *14*, 2759−2770.
(44) Friedrich, M.; Teschner, D.; Knop-Gericke, A.; Armbrüster, M. *J. Phys. Chem. C* **2012**, *116*, 14930−14935.
(45) Yang, B.; Burch, R.; Hardacre, C.; Headdock, G.; Hu, P. *ACS Catal.* **2012**, *2*, 1027−1032.
(46) Huang, L.; Qin, Z.; Wang, G.; Du, M.; Ge, H.; Li, X.; Wu, Z.; Wang, J. *Ind. Eng. Chem. Res.* **2010**, *49*, 4670−4675.
(47) Huang, L.; Wang, G.; Qin, Z.; Dong, M.; Du, M.; Ge, H.; Li, X.; Zhao, Y.; Zhang, J.; Hu, T.; Wang, J. *Appl. Catal., B* **2011**, *106*, 26−38.
(48) Petzold, F. G.; Jasinski, J.; Clark, E. L.; Kim, J. H.; Absher, J.; Toufar, H.; Sunkara, M. K. *Catal. Today* **2012**, *198*, 219−227.
(49) Ryzhikov, A.; Bezverkhyy, I.; Bellat, J.-P. *Appl. Catal., B* **2008**, *84*, 766−772.
(50) Chupas, P. J.; Qiu, X.; Hanson, J. C.; Lee, P. L.; Grey, C. P.; Billinge, S. J. L. *J. Appl. Crystallogr.* **2003**, *36*, 1342−1347.
(51) Hammersley, A. P.; Svensson, S. O.; Hanfland, M.; Fitch, A. N.; Hausermann, D. *High Pressure Res.* **1996**, *14*, 235−248.
(52) Qiu, X.; Thompson, J. W.; Billinge, S. J. L. *J. Appl. Crystallogr.* **2004**, *37*, 678−678.
(53) Farrow, C. L.; Juhas, P.; Liu, J. W.; Bryndin, D.; Božin, E. S.; Bloch, J.; Th, P.; Billinge, S. J. L. *J. Phys.: Condens. Matter* **2007**, *19*, 335219.
(54) Newville, M. *J. Synchrotron Radiat.* **2001**, *8*, 322−324.
(55) Ravel, B.; Newville, M. *J. Synchrotron Radiat.* **2005**, *12*, 537−541.
(56) Malinowski, E. R. *Factor analysis in chemistry*. 3rd ed.; Wiley: New York, 2002; p *xviii*, 414 p.
(57) Wang, Q.; Hanson, J. C.; Frenkel, A. I. *J. Chem. Phys.* **2008**, *129*, 234502−234507.
(58) Neylon, M. K.; Marshall, C. L.; Kropf, A. J. *J. Am. Chem. Soc.* **2002**, *124*, 5457−5465.
(59) Gaskell, K. J.; Starace, A.; Langell, M. A. *J. Phys. Chem. C* **2007**, *111*, 13912−13921.
(60) Rubio-Marcos, F.; Manzano, C. V.; Reinosa, J. n. J.; Romero, J. J.; Marchet, P.; Martín-González, M. S.; Fernández, J. F. *J. Phys. Chem. C* **2011**, *115*, 13577−13583.
(61) Okamoto, H. *J. Phase Equilib.* **2003**, *24*, 280−281.

DOI: 10.1021/acscatal.5b00627
ACS Catal. 2015, 5, 3304−3315